Transport Study of Charge-Carrier Scattering in Monolayer WSe$_2$

Andrew Y. Joe[1,2] Kateryna Pistunova[1] Kristen Kaasbjerg[3] Ke Wang[1] Bumho Kim[4] Daniel A. Rhodes[4]
Takashi Taniguchi[5] Kenji Watanabe[5] James Hone[4] Tony Low[6] Luis A. Jauregui[7] and Philip Kim[1,*]

[1]*Department of Physics, Harvard University, Cambridge, Massachusetts 02138, USA*
[2]*Department of Physics and Astronomy, University of California, Riverside, California 92521, USA*
[3]*Nordea Markets, Nordea Bank Abp, DK-2300 København S, Denmark*
[4]*Department of Mechanical Engineering, Columbia University, New York, New York 10027, USA*
[5]*National Institute for Materials Science, Tsukuba, Japan*
[6]*Department of Electrical and Computer Engineering, University of Minnesota, Minneapolis, Minnesota 55455, USA*
[7]*Department of Physics and Astronomy, The University of California, Irvine, California 92697, USA*

Employing flux-grown single crystal WSe$_2$, we report charge-carrier scattering behaviors measured in h-BN encapsulated monolayer field effect transistors. We observe a nonmonotonic change of transport mobility as a function of hole density in the degenerately doped sample, which can be explained by energy dependent scattering amplitude of strong defects calculated using the T-matrix approximation. Utilizing long mean-free path (> 500 nm), we also demonstrate the high quality of our electronic devices by showing quantized conductance steps from an electrostatically defined quantum point contact, showing the potential for creating ultrahigh quality quantum optoelectronic devices based on atomically thin semiconductors.

Two-dimensional (2D) monolayers of transition metal dichalcogenides (TMDs) hold great promise for future electronics and optoelectronics [1–4]. Because of their strong spin-valley coupling [5,6], they are potential candidates for spin- and valleytronics applications for which high-mobility samples with long spin and valley lifetimes are essential. Progress toward using TMDs for engineering applications or exploring strongly correlated quantum Hall states have been hindered by low carrier mobilities in comparison to other 2D electron gas systems such as graphene or GaAs [7,8]. Similar to conventional 2D semiconductor heterostructure systems, experimental low-temperature mobilities in monolayer TMDs are most often limited by short-range and Coulomb disorder scattering [9–17], and have only recently reached values exceeding 1000 cm^{-2}/(V s) [18–22].

Improvements in the quality of TMD materials have been made utilizing a flux growth technique, decreasing the density of point defects in WSe$_2$ from 10^{13} cm^{-2} to below 10^{11} cm^{-2} [23,24]. Initial transport measurements in these samples have reported mobilities reaching 840 cm^2/(V s) at room temperature and exceeding $44\,000$ cm^2/(V s) at low temperatures [24]. These improvements over crystals grown by the previously conventional chemical vapor transport (CVT) method have shown to be critical for realizing strongly correlated physics in TMD monolayers and heterostructures [20,25–27].

In this Letter, we demonstrate unprecedented transport properties in archetypal monolayer WSe$_2$ based devices fabricated with CVT and flux growth crystals showing ultrahigh mobilities. We measure hole mobilities as large as $25\,000$ cm^2/(V s) for flux-grown samples at low temperatures, whereas we are limited to ~ 3000 cm^2/(V s) in the CVT samples. Interestingly, the mobility (μ) in both CVT and flux-grown crystals shows an unconventional dependence on the carrier density (n), which increases at low n while decreasing at high n. The nonmonotonic behavior of the mobility with n, not expected for long-ranged Coulomb scatterers [28], suggests that transport is dominated by short-range scatterers at high densities [29].

By inspecting the transport and quasiparticle (quantum) scattering times obtained from the measured Hall mobility and quantum oscillations, we show that the transport characteristics are consistent with a nontrivial interplay between (i) disorder scattering due to *intrinsic* atomic defects, such as, e.g., commonly encountered atomic vacancies, and (ii) scattering by *extrinsic* (remote) charge impurities in the substrate. This manifests itself in the peculiar situation where, at low temperatures, the transport lifetime is limited by the former, while the quantum lifetime is limited by the latter (new paradigm).

We fabricate dual graphite gated, h-BN encapsulated single layer WSe$_2$ devices with prepatterned platinum (Pt) contacts [18,30]. We transfer the monolayer WSe$_2$ on top of the prepatterned Pt contacts, which has a high work function that matches the valence band edge of WSe$_2$ [see Supplemental Material (SM) [31] for contact engineering details]. We use thin, optically transparent graphite
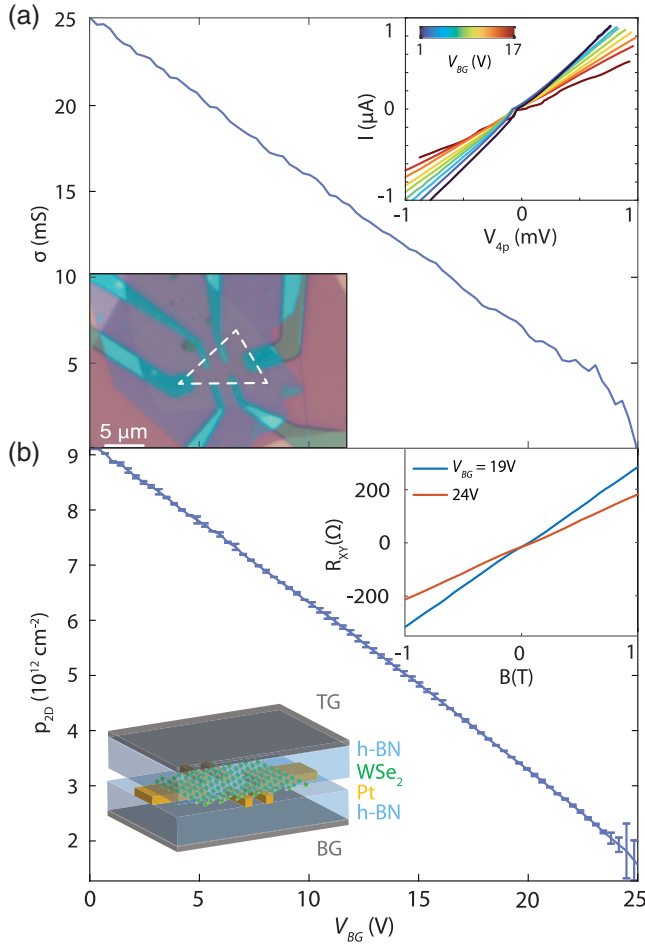
FIG. 1. (a) Conductivity σ measured at $T = 1.5$ K with back gate voltage V_{BG}. Upper inset: four-probe IV curves taken at $T = 1.5$ K at different values of V_{BG} while applying a large negative V_{TG} to dope the contact area. The linearity of IV curves proves ohmic p-type contact to single layer WSe$_2$ at cryogenic temperatures. Lower inset: optical image of a representative device with top and bottom graphite gates and prepatterned Pt contacts. WSe$_2$ monolayer is outlined in white dashed line. (b) Hole density obtained from Hall measurements, with V_{BG}. Upper inset: representative transverse resistance R_{xy} curves at different V_{BG} with magnetic field B. Lower inset: cross-section cartoon of a representative device.

gates to allow optical access to the WSe$_2$ flake. We use high quality h-BN crystals with low intrinsic defect densities ($< 3 \times 10^8$ cm^{-2}) as the substrate and gate dielectric [35]. The thickness of top and bottom h-BN gate dielectric is 50 and 73 nm, respectively [the lower inset of Figs. 1(a) and 1(b)].

To activate the contacts, we apply a top gate voltage of $V_{TG} = -23.1$ V, doping the TMD flake in the channel and in the contact area. Since the bottom gate is screened by the prepatterned electrodes, we can tune the channel carrier density using the bottom gate while maintaining high contact doping. The upper inset of Fig. 1(a) shows linear four-probe (V_{4p}) IV curves at different channel carrier

densities at 1.5 K, demonstrating Ohmic p-type contacts to monolayer WSe$_2$ at cryogenic temperatures. By highly doping the contact area and using prepatterned Pt contacts, we achieve a low barrier for injecting holes. Ohmic contacts to single layer WSe$_2$ allow us to study its magnetotransport. To extract transport mobility, we measure conductivity at different bottom gate voltages (V_{BG}), as shown in Fig. 1(a). In Fig. 1(b), we obtain the hole density (p_{2D}) from Hall measurements at different gate voltages. The linearity of the transverse resistance R_{xy} curves further proves the quality of the electrical contact and gives us a lower limit for our tunable doping of $p_{2D} \approx 1.5 \times 10^{12}$ cm^{-2}.

Under a perpendicular magnetic field (B) our samples exhibit Shubnikov–de Haas (SdH) oscillations. Figure 2(a) shows a Landau fan diagram with longitudinal resistance R_{xx} measured at $T = 1.5$ K as a function of bottom gate V_{BG} in fields up to 13.5 T. The switching between even and odd integer denominator Landau level (LL) observed in the fan diagram, consistent with previous studies, arises due to the interplay between the Zeeman splitting and the cyclotron energy [18,20]. If the Zeeman splitting is equal to or larger than the cyclotron energy, the LL sequence changes depending on the E_Z/E_c ratio. A ratio close to an even (odd) integer leads to a sequence that is dominated by odd (even) states. Figure 2(b) show line cuts of the longitudinal resistance R_{xx} vs inverse magnetic field at V_{BG} voltages corresponding to the dashed lines in Fig. 2(a). Figure 2(c) shows the corresponding Fourier transform amplitude vs frequency, showing the principle frequency (f) and its second harmonic ($2f$), revealing the even-odd effect mentioned above. We calculate the SdH density $p_{SdH} = (2e/h)f$, which agrees well with a LL degeneracy of 2 (i.e., $p_{2D} = 2p_{SdH}$). Figure 2(d) shows ΔR_{xx} vs $1/B$ from the CVT device (see SM [31]) at different temperatures, which we fit to the Dingle factor to extract a hole effective mass $m^* = 0.35m_0$, close to the value obtained in a previous study [18].

From the Dingle analysis of SdH oscillation amplitude vs $1/B$, we extract the quantum scattering lifetime τ_q and compare it with the transport scattering lifetime τ, estimated from $\tau = \sigma m^*/e^2 p_{2D}$, as function of hole carrier density p_{2D} [Fig. 2(e)]. We find that both τ and τ_q increase with decreasing density for $p_{2D} > p_* = 2 \times 10^{12}$ cm^{-2}, reaching the maximum values, ~6000 fs and ~450 fs, respectively. Below p_*, τ decreases steeply as p_{2D} decreases further, while τ_q cannot be estimated in this regime due to disappearance of the SdH oscillation.

The observed behavior of τ and τ_q suggests that there is an intricate interplay between the short-range and long-range scatterers in our samples. First, the decreasing τ with decreasing $p_{2D} < p_*$ suggests that the long-ranged charged Coulomb scatterers dominate in this lower density regime as the carrier screening becomes weaker. Similar behaviors of τ in the low density limit was obtained in the commercially obtained CVT grown crystals (see SM [31]),
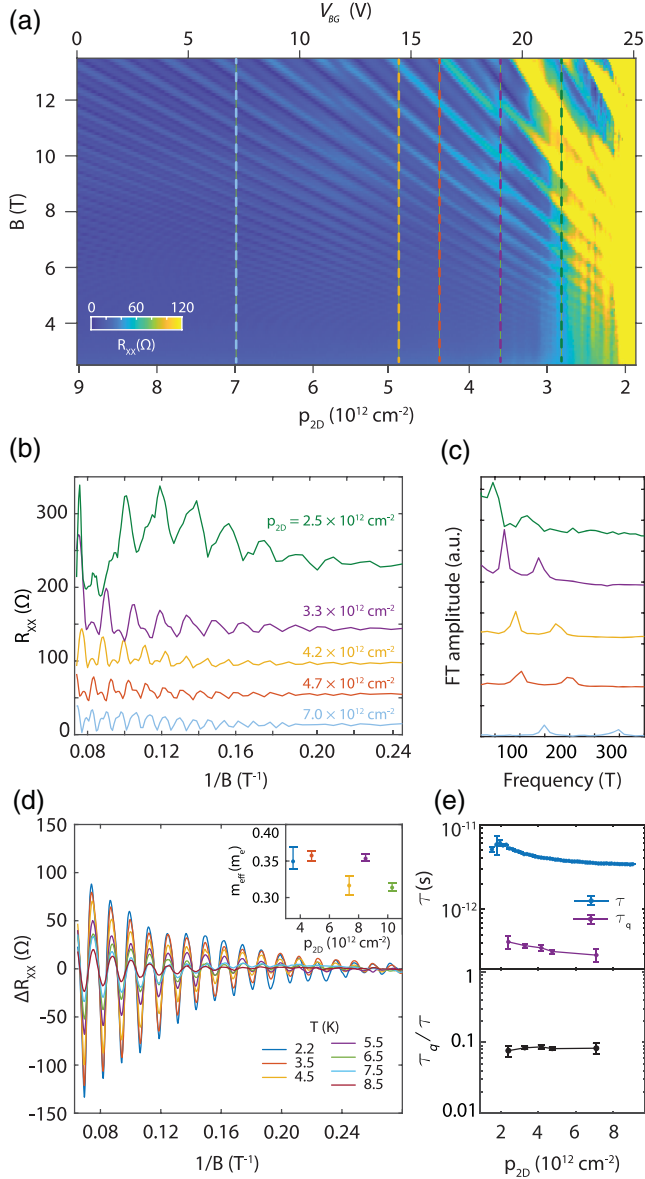
FIG. 2. (a) Landau fan diagram of longitudinal resistance R_{xx} measured at $T = 1.5$ K as a function of bottom gate V_{BG} voltage and magnetic field. Dashed lines correspond to line cuts in (b). (b) R_{xx} for different bottom gate voltages as a function of the inverse magnetic field $(1/B)$. (c) Fourier transform amplitude with frequency, spaced proportionally to back gate voltage. Colors correspond to the data in (b). (d) Change in longitudinal resistance ΔR_{xx} of a CVT device as a function of the inverse of magnetic field measured at various temperatures. Inset: effective hole mass with hole density. (e) Top: transport scattering lifetime, τ, and quantum scattering lifetime, τ_q, as a function of hole density. Bottom: ratio τ_q/τ of quantum scattering lifetime to transport scattering lifetime as a function of hole density.

FIG. 3. (a) Transport mobility μ as a function of temperature for fixed hole densities. Dashed lines show $\mu \sim T^{-\gamma}$ for $\gamma = 1, 3/2$ as a guide. (b) Transport mobility μ as a function of hole density for different temperatures. (c) T-matrix calculations of the mobility as a function of density for various temperatures showing qualitative agreement.

although p_* in this lower quality sample tends to be much higher than that of the flux-grown samples. Since both the flux-grown and CVT samples were measured with a similar device geometry, we speculate the unscreened long-range
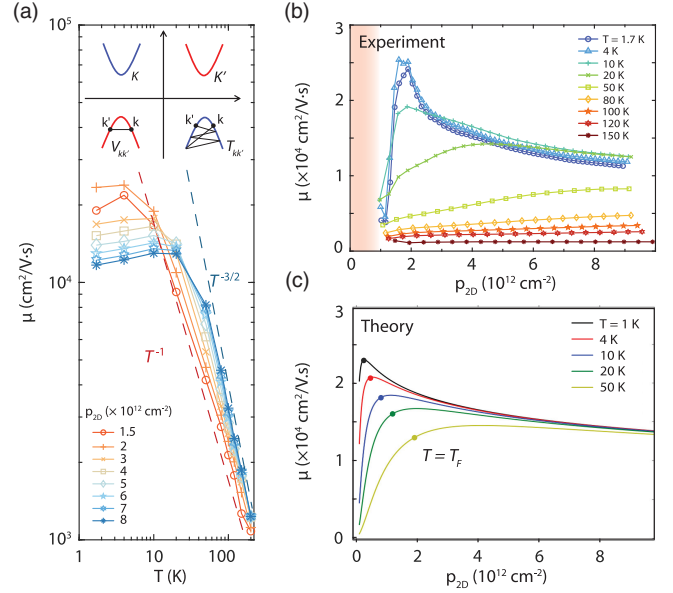
scatterers are likely extrinsic to the WSe$_2$ channels. Second, decreasing τ and τ_q in the higher density regime, $p_{2D} > p_*$, suggests a strong energy dependent scattering rate for short-range scatterers. We note that in this high density limit, the long-range Coulomb scatters are screened, leaving only the effect of short-range scatterers. We note that a weak first order perturbation based Born approximation yields $\tau \sim \tau_q$, and both τ and τ_q remain density independent [29]. However, our experimental observation clearly indicates that both τ and τ_q decreases with increasing p_{2D}, while $\tau_q/\tau \sim 0.1$. This unusual trends of scattering times, thus, suggest that one needs to consider the effect of strong short-range scatterers beyond the Born approximation [36,37].

Further evidence for strong short-range scattering potentials are shown in the study of temperature dependent transport mobility. Figure 3(a) displays transport mobility plotted as a function of temperature for fixed hole densities. The observed $\mu \sim T^{-\gamma}$ dependence at higher temperatures is a manifestation of optical phonon scattering and the exponent γ can be used to characterize the dominating phonon scattering mechanism [38]. At the lowest densities, the mobility scales with $\gamma \sim 1$, indicating acoustic phonon scattering above the Bloch-Grüneisen temperature. For higher densities, we observe an increased exponent of $\gamma \sim 3/2$, indicating a transition into optical phonon scattering through the deformation potential couplings and Fröhlich interaction [38]. At lower temperatures, however, mobility tends to grow more slowly as T decreases, due to

the diminishing role of electron-phonon scattering over impurity scattering. At this low temperature limit where the impurity scattering becomes appreciable, we find $\mu(T)$ exhibits a complicated behavior, including nonmonotonic change with T at the high density limit. The origin of this density dependent anomalous mobility modulation at low temperatures can be related to the scattering rate τ^{-1} change with density p_{2D} discussed above.

Figure 3(b) shows transport mobility μ vs hole density at different temperatures, calculated from the measured Hall density p_{2D} and conductivity σ. μ reaches the maximum value $\sim 25\,000$ cm^2/(V s) at 4 K and $p \approx p_* \sim 2 \times 10^{12}$ cm^{-2}. This high mobility is consistent with optical studies of high quality WSe$_2$ devices, where in photoluminescence measurements we observe narrow linewidths and emission of complex excitonic states [39,40]. As T increases, the density where μ (and corresponding τ) is peaked, $p_*(T)$, increases rapidly. For higher temperatures, $T > 50$ K, we recover the typical mobility vs density dependence, i.e., monotonically decreasing μ as p_{2D} decreases due to the increasing contribution of unscreened charged defects. We observe a similar mobility vs hole density trend in commercial CVT crystals (see SM [31]), but with an order of magnitude lower mobility of ~ 3000 cm^2/(V s) at 4 K. While the lower mobility is attributed to higher defect density in CVT crystals, the unconventional mobility behavior in both crystals suggests that hole transport in WSe$_2$ monolayers is intrinsically different than in conventional semiconductors that are limited by charged impurities.

The strong density dependence of the mobility indicates a concomitant breakdown of the Born approximation for intrinsic defects. Such a failure of the Born approximation occurs in graphene where quasibound defect states near the Dirac point generate resonant scattering and a nontrivial density dependence of the mobility [41–44]. However, in monolayer WSe$_2$, we here find that the density dependence of the mobility can be traced back to a pronounced *renormalization* of the Born scattering amplitude by 1–2 orders of magnitude due to the strong impurity strength of vacancies [36].

For quantitative comparison with experimental data, we perform T-matrix calculations, which can be used to incorporate intrinsic point defects and remote charge impurities (see SM [31] for more detail) [36]. A transport model for μ was implemented in a separate work [37], which accounts for both charge neutral point defects and remote charge impurities, the temperature dependent 2D electron gas screening of the latter, and the finite temperature electron Fermi distributions (see SM [31] for temperature dependent details). Because of larger spin-orbit splitting in the WSe$_2$ valence bands than the hole filling level, intrinsic intravalley scattering dominates over the energetically unfavorable intervalley scattering [Fig. 3(a) inset]. Then, we find that unconventional increase of the mobility for decreasing density is well captured by short-range impurity scattering from charge neutral point defects. To capture the sharp decrease of the mobility at the lowest

densities ($p_{2D} < p_*$), we include remote charge impurities, which become relevant at lower carrier mobilities with less screening. Figure 3(c) shows the calculated mobility as a function of p_{2D} and temperature where we have strong agreement between the theory and experimental results. We estimate an intrinsic impurity density of around 10^{11} cm^{-2} for flux-grown crystals and 10^{12} cm^{-2} for CVT samples, consistent with STM studies of the bulk TMD crystals [23]. In both cases, the concentration of remote charge (Coulomb) impurities is around 10^{12} cm^{-2}. These calculations strongly suggest that WSe$_2$ is not limited by charged defects, but rather intrinsic, short-ranged charge-neutral defects in the system. We note that the mobility's dependence on density at low temperatures is consistent in both flux-grown and CVT devices (see SM [31]), implying this is the limiting scattering mechanism for hole transport in WSe$_2$ devices regardless of the defect densities. Density functional theory calculations of mid-gap states induced by point defects at either the W or Se sites show a limited density of states for Se vacancies [36].

The high mobility we achieve at $p_{2D} = p_*$ corresponds to the carrier mean-free path reaching ~ 500 nm in monolayer WSe$_2$. This long mean-free path enables us to build an electrically controlled quantum point contact (QPC) device using local back gates. In Fig. 4(a), we show an atomic
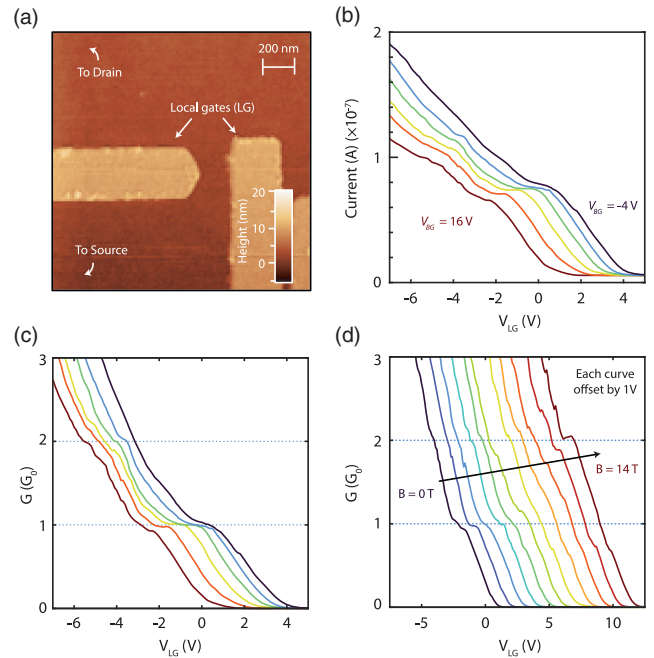
FIG. 4. (a) Atomic force microscopy image the local gates (V_{LG}) used to form a quantum point contact (QPC). (b) Line cuts of the current as a function of V_{LG} for different V_{BG}, showing quantized conductance as the QPC is pinched off. (c) Same line cuts plotted in units of quantum conductance (G_0) with subtraction of series resistance (R_s), parallel resistance from uncontrolled regions (R_0), and V_{bias} reduction due to Schottky barrier effects. (d) Line cuts of conductance as a function of V_{LG} for various B at $V_{BG} = 5$ V.

force microscopy image of the local gate structure in such a device. A 2D hole gas is generated at $T = 1.7$ K by electrostatic gating with the contact gates and a global back gate and the potential of the two local gates are shifted together to deplete carriers and create a constriction less than ~ 200 nm for quantum confinement. Figure 4(b) shows the measured current across the device as a function of the local gate voltage (V_{LG}) for different back gate voltages (V_{BG}) with a 300 mV alternating current bias. The current exhibits plateaulike features in the current stemming from quantized conductance as the channel width of the QPC approaches the Fermi wavelength. The measured current can be converted to QPC conductance, after subtracting off the series resistances and leakage current in the local gate area (see SM [31] for more detailed procedure). Figure 4(c) shows the QPC conductance corresponding to the data in Fig. 4(b). At least two well-defined conductance plateaus, corresponding to integer steps of $G_0 = 2e^2/h$, are visible as the QPC constriction becomes wider at lower V_{LG}. We find that upon applying perpendicular magnetic fields, these plateaus split [Fig. 4(d)]. The emergence of two additional conductance steps suggests a lifting of the degenerate spin-locked K valley valence bands at high magnetic fields.

In conclusion, we report high mobility charge transport in low defect density monolayer WSe$_2$, where the mobility is limited by electron-phonon scattering at high temperatures and by intricate interplay between short- and long-range scatters at low temperatures, reaching up to 500 nm carrier mean-free path at an optimized carrier density. We demonstrate that high quality electronic devices are possible by showing quantized conductance steps from an electrostatically defined quantum point contact, opening a doorway for quantum electronic devices based on mono-layer TMDs. Extending similar studies to other semiconducting TMDs will offer a doorway for quantum electronics based on atomically thin semiconductors.

---

*Corresponding author: philipkim@g.harvard.edu

[1] K. F. Mak, C. Lee, J. Hone, J. Shan, and T. F. Heinz, Phys. Rev. Lett. **105**, 136805 (2010).

[2] B. Radisavljevic, A. Radenovic, J. Brivio, V. Giacometti, and A. Kis, Nat. Nanotechnol. **6**, 147 (2011).

[3] T. Korn, S. Heydrich, M. Hirmer, J. Schmutzler, and C. Schüller, Appl. Phys. Lett. **99**, 102109 (2011).

[4] P. Avouris, T. F. Heinz, and T. Low, *2D Materials* (Cambridge University Press, Cambridge, England, 2017).

[5] D. Xiao, G.-B. Liu, W. Feng, X. Xu, and W. Yao, Phys. Rev. Lett. **108**, 196802 (2012).

[6] X. X. W. Yao, D. Xiao, and T. F. Heinz, Nat. Phys. **10**, 343 (2014).

[7] C. R. Dean, A. F. Young, I. Meric, C. Lee, L. Wang, S. Sorgenfrei, K. Watanabe, T. Taniguchi, P. Kim, K. L. Shepard, and J. Hone, Nat. Nanotechnol. **5**, 722 (2010).

[8] Y. J. Chung, K. A. V. Rosales, K. W. Baldwin, P. T. Madathil, K. W. West, M. Shayegan, and L. N. Pfeiffer, Nat. Mater. **20**, 632 (2021).

[9] B. Radisavljevic and A. Kis, Nat. Mater. **12**, 815 (2013).

[10] B. W. H. Baugher, H. O. H. Churchill, Y. Yang, and P. Jarillo-Herrero, Nano Lett. **13**, 4212 (2013).

[11] W. Zhu, T. Low, Y.-H. Lee, H. Wang, D. B. Farmer, J. Kong, F. Xia, and P. Avouris, Nat. Commun. **5**, 3087 (2014).

[12] Z. Yu, Y. Pan, Y. Shen, Z. Wang, Z.-Y. Ong, T. Xu, R. Xin, L. Pan, B. Wang, L. Sun, J. Wang, G. Zhang, Y. W. Zhang, Y. Shi, and X. Wang, Nat. Commun. **5**, 5290 (2014).

[13] H. Schmidt, S. Wang, L. Chu, M. Toh, R. Kumar, W. Zhao, A. H. C. Neto, J. Martin, S. Adam, B. Özyilmaz, and G. Eda, Nano Lett. **14**, 1909 (2014).

[14] L. Chu, H. Schmidt, J. Pu, S. Wang, B. Özyilmaz, T. Takenobu, and G. Eda, Sci. Rep. **4**, 7293 (2014).

[15] X. Cui, G.-H. Lee, Y. D. Kim, G. Arefe, P. Y. Huang, C.-H. Lee, D. A. Chenet, X. Zhang, L. Wang, F. Ye, F. Pizzocchero, B. S. Jessen, K. Watanabe, T. Taniguchi, D. A. Muller, T. Low, P. Kim, and J. Hone, Nat. Nanotechnol. **10**, 534 (2015).

[16] H. Schmidt, I. Yudhistira, L. Chu, A. H. C. Neto, B. Özyilmaz, S. Adam, and G. Eda, Phys. Rev. Lett. **116**, 046803 (2016).

[17] X. Cui, E.-M. Shih, L. A. Jauregui, S. H. Chae, Y. D. Kim, B. Li, D. Seo, K. Pistunova, J. Yin, J.-H. Park, H.-J. Choi, Y. H. Lee, K. Watanabe, T. Taniguchi, P. Kim, C. R. Dean, and J. C. Hone, Nano Lett. **17**, 4781 (2017).

[18] B. Fallahazad, H. C. Movva, K. Kim, S. Larentis, T. Taniguchi, K. Watanabe, S. K. Banerjee, and E. Tutuc, Phys. Rev. Lett. **116**, 086601 (2016).

[19] R. Pisoni, Z. Lei, P. Back, M. Eich, H. Overweg, Y. Lee, K. Watanabe, T. Taniguchi, T. Ihn, and K. Ensslin, Appl. Phys. Lett. **112**, 123101 (2018).

[20] M. V. Gustafsson, M. Yankowitz, C. Forsythe, D. Rhodes, K. Watanabe, T. Taniguchi, J. Hone, X. Zhu, and C. R. Dean, Nat. Mater. **17**, 411 (2018).

[21] S. Larentis, H. C. P. Movva, B. Fallahazad, K. Kim, A. Behroozi, T. Taniguchi, K. Watanabe, S. K. Banerjee, and E. Tutuc, Phys. Rev. B **97**, 201407(R) (2018).

[22] R. Pisoni, A. Kormányos, M. Brooks, Z. Lei, P. Back, M. Eich, H. Overweg, Y. Lee, P. Rickhaus, K. Watanabe, T. Taniguchi, A. Imamoglu, G. Burkard, T. Ihn, and K. Ensslin, Phys. Rev. Lett. **121**, 247701 (2018).

[23] D. Edelberg, D. Rhodes, A. Kerelsky, B. Kim, J. Wang, A. Zangiabadi, C. Kim, A. Abhinandan, J. Ardelean, M. Scully, D. Scullion, L. Embon, R. Zu, E. J. Santos, L. Balicas, C. Marianetti, K. Barmak, X. Zhu, J. Hone, and A. N. Pasupathy, Nano Lett. **19**, 4371 (2019).

[24] S. Liu, Y. Liu, L. N. Holtzman, B. Li, M. Holbrook, J. Pack, T. Taniguchi, K. Watanabe, C. R. Dean, A. Pasupathy, K. Barmak, D. A. Rhodes, and J. Hone, arXiv:2303.16290.

[25] Q. Shi, E. M. Shih, M. V. Gustafsson, D. A. Rhodes, B. Kim, K. Watanabe, T. Taniguchi, Z. Papić, J. Hone, and C. R. Dean, Nat. Nanotechnol. **15**, 569 (2020).

[26] L. Wang, E. M. Shih, A. Ghiotto, L. Xian, D. A. Rhodes, C. Tan, M. Claassen, D. M. Kennes, Y. Bai, B. Kim, K. Watanabe, T. Taniguchi, X. Zhu, J. Hone, A. Rubio, A. N. Pasupathy, and C. R. Dean, Nat. Mater. **19**, 861 (2020).

[27] Q. Shi, E. M. Shih, D. Rhodes, B. Kim, K. Barmak, K. Watanabe, T. Taniguchi, Z. Papić, D. A. Abanin, J. Hone, and C. R. Dean, Nat. Nanotechnol. **17**, 577 (2022).

[28] S. Das Sarma and E. H. Hwang, Phys. Rev. B **88**, 035439 (2013).

[29] S. Das Sarma and E. H. Hwang, Phys. Rev. B **89**, 121413(R) (2014).

[30] L. A. Jauregui, A. Y. Joe, K. Pistunova, D. S. Wild, A. A. High, Y. Zhou, G. Scuri, K. De Greve, A. Sushko, C.-H. Yu, T. Taniguchi, K. Watanabe, D. J. Needleman, M. D. Lukin, H. Park, and P. Kim, Science **366**, 870 (2019).

[31] See Supplemental Material at http://link.aps.org/supplemental/10.1103/PhysRevLett.132.056303 for additional details on contact engineering, data from CVT samples, theory for the transport and scattering models, and QPC measurements, which includes Refs. [32–34].

[32] P. F. Maldague, Surf. Sci. **73**, 296 (1978).

[33] T. Ando, A. B. Fowler, and F. Stern, Rev. Mod. Phys. **54**, 437 (1982).

[34] K. Flensberg and B. Y.-K. Hu, Phys. Rev. B **52**, 14796 (1995).

[35] T. Taniguchi and K. Watanabe, J. Cryst. Growth **303**, 525 (2007).

[36] K. Kaasbjerg, Phys. Rev. B **101**, 045433 (2020).

[37] K. Kaasbjerg, T. Low, and A.-P. Jauho, Phys. Rev. B **100**, 115409 (2019).

[38] K. Kaasbjerg, K. S. Thygesen, and K. W. Jacobsen, Phys. Rev. B **85**, 115317 (2012).

[39] Z. Li, T. Wang, Z. Lu, C. Jin, Y. Chen, Y. Meng, Z. Lian, T. Taniguchi, K. Watanabe, S. Zhang, D. Smirnov, and S. F. Shi, Nat. Commun. **9**, 3719 (2018).

[40] M. Barbone, A. R. Montblanch, D. M. Kara, C. Palacios-Berraquero, A. R. Cadore, D. De Fazio, B. Pingault, E. Mostaani, H. Li, B. Chen, K. Watanabe, T. Taniguchi, S. Tongay, G. Wang, A. C. Ferrari, and M. Atatüre, Nat. Commun. **9**, 3721 (2018).

[41] P. M. Ostrovsky, I. V. Gornyi, and A. D. Mirlin, Phys. Rev. B **74**, 235443 (2006).

[42] D. M. Basko, Phys. Rev. B **78**, 115432 (2008).

[43] J. P. Robinson, H. Schomerus, L. Oroszlány, and V. I. Fal'ko, Phys. Rev. Lett. **101**, 196803 (2008).

[44] T. O. Wehling, S. Yuan, A. I. Lichtenstein, A. K. Geim, and M. I. Katsnelson, Phys. Rev. Lett. **105**, 056802 (2010).